PONTIFICIA UNIVERSIDAD CATÓLICA DEL PERÚ

FACULTAD DE CIENCIAS E INGENIERÍA

A study of Ultra-High-Energy Cosmic Ray propagation in one-dimensional simulations

TRABAJO DE INVESTIGACIÓN PARA LA OBTENCIÓN DEL GRADO DE BACHILLER EN CIENCIAS CON MENCIÓN EN FÍSICA

AUTOR

Jose Gabriel Olivares Schneider

ASESOR

Dr. José Luis Bazo Alba

Lima, Enero, 2021

Abstract

Cosmic Rays have come to play an important role in understanding the universe, and astroparticle physics has undergone major developments in the last few decades. As such, several observatories have been set up with the purpose of detecting these particles, and simulation frameworks have been developed in order to further analyze their behavior by creating highly variable environments and parameters.

This work covers the essential theory required to study propagation of Ultra-High-Energy Cosmic Rays restricted to linear one-dimensional propagation only; this includes the primary methods of energy loss during propagation, mainly through reactions with the photon background like photo-pion production and photo-disintegration, and additional cosmological effects. The study was done using the CRPropa 3.0 simulation framework. To determine the best possible maximum energy for the simulations, initial trials were done by testing the GZK cutoff for multiple energy values, followed by an analysis of heavier nuclei propagation.

As a final complete test run, a model of the cosmic ray spectrum for energies above 10^{18} eV was made based on two data sets, one made from the average composition of the whole CR energy spectrum, and the other from The Pierre-Auger Observatory measurements for the high energy range. The results showed that initial source composition was the determining factor in the shape of the CR spectrum. These initial simulations done in this work will set the ground for future more complex simulations and studies.

Resumen

Los rayos cósmicos juegan un papel importante en nuestro entendimiento del universo, por eso, la física de astropartículas ha sido desarrollada en gran medida en estas últimas décadas. Varios observatorios han sido construidos con el propósito de detectar estas partículas, y a su vez se han desarrollado programas de simulaciones para analizar su compartamiento usando ambientes y variables con una alta variabilidad.

Este trabajo cubre la teoría necesaria para estudiar la propagación de rayos cósmicos de ultra-altas energías restringido a una sola dimensión; esto incluye las principales causas de pérdida de energía durante su propagación, principalmente a través de interacciones con el fondo de fotones como la fotoproducción de piones y fotodesintegración, así como otros efectos cosmológicos. Este estudio fue realizado con el programa de simulaciones CRPropa 3.0. Para determinar la mejor energía máxima para las simulaciones, los primeros ensayos comprobaron el límite GZK para múltiples valores de energía, seguido de un análisis de la propagación de núcleos más pesados.

A manera de ensayo final, un modelo del espectro de rayos cósmicos para energías mayores a 10^{18} eV fue hecho basado en dos grupos de datos, uno a partir de la composición general promedio de todo el espectro de energías de los rayos cósmicos, y el otro a partir de mediciones hechas por el observatorio Pierre-Auger para altas energías. Los resultados muestran que la composición inicial de la fuente es el factor determinante en la forma del espectro. Las simulaciones iniciales hechas en este trabajo serán utilizadas como base para futuras y más complejas investigaciones.

Acknowledgements

I would like to acknowledge the developers of CRPropa for making the code publicly available. I wish to express my deepest gratitude to my advisor, Prof. Bazo, for his feedback and guidance for this research; and a special thanks to all friends and colleagues whose support and assistance helped me in the completion of this project.

Contents

Chapter 1

Introduction

Particle physics is one of the fundamental pillars of modern science and has undergone significant advancements in the twentieth century, which resulted in many different new fields of research being opened for study. Astroparticle physics evolved into one of these new branches, combining major elements from high energy physics and astrophysics, as well as others, and is concerned with understanding the key elements in our universe and its creation by studying the highly energetic particles arriving from space called Cosmic Rays (CRs). Over the last few decades, advanced methods of detection and data management have helped develop the field at a rapid pace in comparison to its beginnings, helping us further our knowledge of space and bringing us one step closer to answering unresolved questions.

The ample variability and processes involved with CRs makes the use of simulation frameworks an appealing option nowadays, as their high versatility allows experiments to be carried out over an immense variation of initial conditions and have control over otherwise random variables. This work will serve to set the basis for future research with simulation software, and as a means

of realizing the maximum potential of these tools. Three-dimensional or four-dimensional simulations contain increasingly complex variables and calculations that can prove to be overwhelming should one not cover the essentials, thus, for simplicity, this work will focus on one-dimensional simulations only, seeking to reach a thorough understanding of the inner workings of the programming framework, and to identify potential bottlenecks and errors.

This Chapter will briefly summarize the historical background of CRs; Chapter 2 will cover the essential background needed to understand one-dimensional simulations, such as primary interactions and energy loss calculations; Chapter 3 will explain the simulation framework used, show the first significant trials, study the GZK cutoff and observe the effects of different simulation energies; Chapter 4 presents a relatively more thorough simulation with plausible results and a simple model of the UHECR flux; and finally Chapter 5 will present the concluding thoughts and some closing statements.

1.1 Discovery of Cosmic Rays

After the discovery of radiation, one of the more pressing questions left to answer was the origin of air ionization. It was widely believed that the sources of this atmospheric electricity were radioactive components found on the Earth's crust. Some early measurements showed that radiation levels actually increased with altitude, and in 1912 an Italian physicist named Domenico Pacini performed a series of measurements over the surface of the sea, a lake, and underwater. Due to the decreasing levels of ionization while underwater, he began

to suspect that radiation levels in the air must not be entirely dependent on materials from the Earth's crust [1]. That same year, Victor Hess did a series of free balloon flights carrying electrometers to measure ionization levels. Some flights were done at night and others were done during a solar eclipse, ruling out the possibility of interference from the sun. Since measurements showed a significant increase in radiation at higher altitudes, it was determined that the source of air ionization must not come from the Earth's crust, instead there must be a highly penetrative power entering our atmosphere from above [2]. Many consider this the starting point of the astroparticle physics research field.

After their discovery, several experiments were carried out to find out more about this unknown radiation. In 1925, Robert Millikan confirmed Hess' findings by performing another series of measurements at different altitudes and with highly specialized equipment. The intensity at higher altitudes indicated that the radiation must have cosmic origins, and given their high penetrative power he assumed they had to be highly energetic electromagnetic waves - gamma rays- and thus was the first to label this particles "cosmic rays" [3].

However, experiments that followed soon after hinted at the contrary. The rays appeared to be deflected by the Earth's geomagnetic field, as evidenced by the gradual increase in radiation levels at higher latitudes [4], this meant that cosmic rays were not photons, but instead were electrically charged particles. This was further demonstrated by follow-up experiments in which other characteristics were discovered. One of the most important ones was proof of the "east-west effect", which showed a certain degree of asymmetry in intensity; measurements showed that cosmic ray numbers were greater from the west, and

this hinted at a composition with predominantly positive electric components [5]. Finally, in 1937, Pierre Auger detected simultaneous signals in separated Geiger counters, which had enough distance between them that the event could not be attributed to circuit delay, and concluded that those signals resulted from a cascade of particles coming from the air. This reaction occurred when cosmic rays interacted with atoms in the air once they entered the atmosphere [6]. These experiments resulted in a new label that depended on the origin of these particles: those coming directly from cosmological sources were called primary cosmic rays, and those that originated in our atmosphere during particle showers were named secondary cosmic rays.

Modern day technology has allowed us to further expand our research capability, and nowadays we have entire experiments specializing in the detection of either primary or secondary cosmic rays. Several international research centers dedicate their entire efforts in collecting data from air showers and other particles; amongst the most prominent we have the Pierre Auger Observatory in Argentina and the Telescope Array project in the United states, which specialize in secondary rays coming from Ultra-High-Energy Cosmic Rays, other observatories include the Major Atmospheric Gamma Imaging Cherenkov Telescopes (MAGIC),the High Energy Stereoscopic System (HESS) or High Altitude Water Cherenkov Observatory (HAWC) which focus on detecting highly energetic gamma rays and finally the IceCube Neutrino Observatory in Antarctica, designed to collect data from astrophysical neutrinos.

Chapter 2

Propagation of Utra-High-Energy Cosmic Rays

2.1 Energy Spectrum and Flux

Throughout the years, different experiments have measured the secondary air showers and primary cosmic rays. The results, as shown in Fig. 1, have yielded a fairly accurate perspective of what the energy spectrum of primary cosmic rays looks like, covering a broad range of energies from several GeV to little over 10^{20} eV. As the energy level increases, a few distinct features start to appear. First the knee at around 10^{15} eV, a smaller second knee at around 10^{17} eV, a flattening of the spectrum at $10^{18} - 10^{19}$ eV and finally a cutoff at around $10^{19} - 10^{20}$ eV. The cause of these features is still investigated, and many scientists provide different explanations on their origins. Data extracted from the Telescope Array Low Energy extension (TALE), for example, seems to suggest that the first knee is caused by a lower amount of metals in the cosmic ray composition and a rise of iron nuclei abundance, and that the second

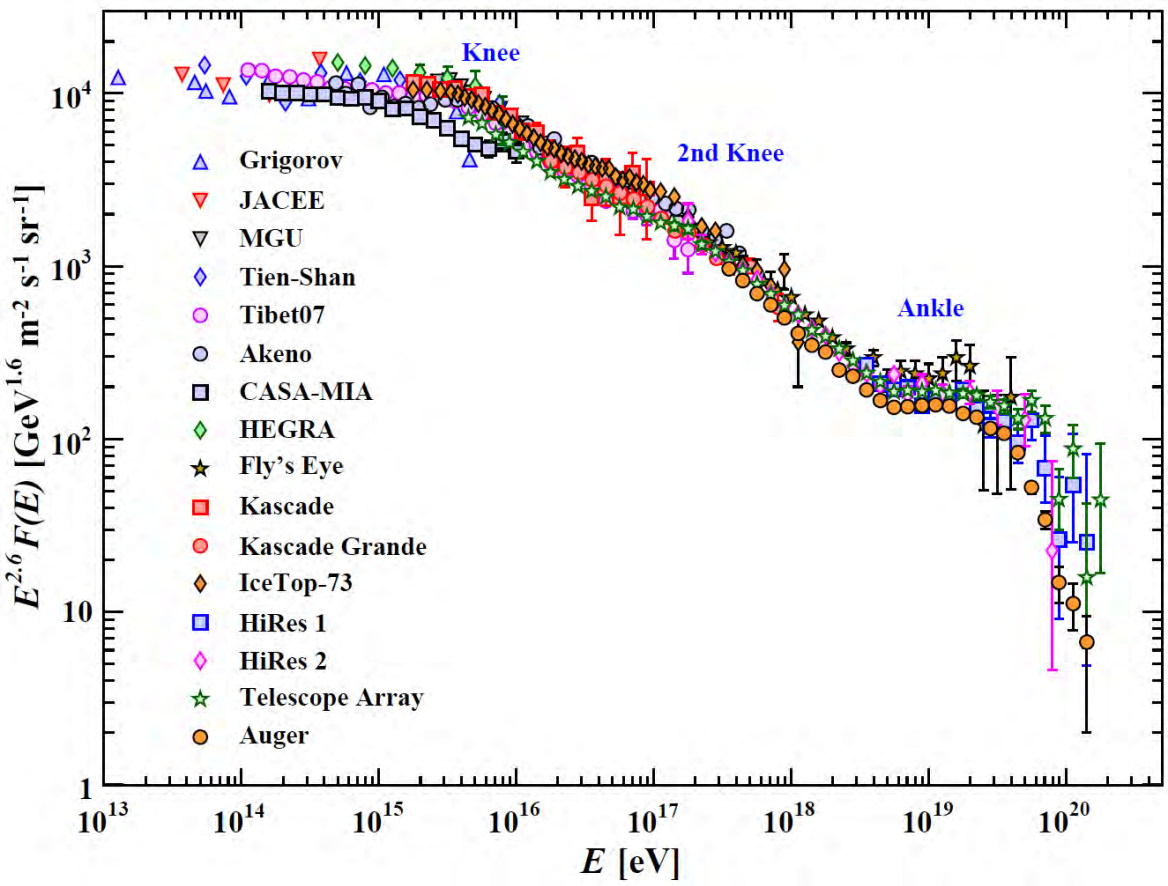

Figure 1: The Cosmic Ray Energy Spectrum. The steepening of the spectrum can be seen at around 10^{15} eV and at 10^{17} eV, corresponding to the first and second knee respectively, the ankle can be seen at around 10^{19} eV [8].

knee shows the very end of the galactic spectrum. Cosmic rays with energies above it are assumed to come from extragalactic sources. [7]. According to authors of the Particle Data Group, the intensity of primary cosmic ray nucleons in the energy range from several GeV to somewhat beyond 10^{14} eV (around the first knee) is given approximately by:

$$\frac{dN}{dE} \simeq 1.8 \times 10^4 E^{-2.7} \frac{\text{nucleons}}{\text{m}^2 \text{ s sr GeV}} \tag{2.1}$$

where E is the energy-per-nucleon (including rest mass energy) [8]. The flux for energies above 10^{14} eV becomes low enough that individual events cannot

be detected directly with small scale detectors. Instead, the properties of the primary particle particles are deduced from detection of the secondary particles produced in extensive air showers [9].

Cosmic rays that have energies beyond 10^{18} eV (or 1 EeV) are labelled Ultra-High-Energy Cosmic Rays (UHECRs). Little is known about their sources, and according to the Pierre Auger Collaboration, at these energies the magnetic fields inside the Milky Way are not strong enough to keep them confined, hence it was hypothesized that the sources of UHECRs must be of extragalactic origin [10]. In 2017 the same group presented further evidence of this hypothesis by analyzing the inconsistencies between the anisotropy in detections and the proposed models with sources in the center of our galaxy [11]. The fact that UHECRs have to travel enormous distances to reach Earth, as well as their different interactions with background radiation, makes them incredibly difficult to trace back to their original source. The following sections will now cover the reactions and energy losses that affect these particles during their propagation in a one-dimensional space.

2.2 Photo-pion production and GZK Limit

One of the most significant features mentioned in the spectrum was the energy cutoff at around $10^{19} - 10^{20}$ eV, the causes of which have been studied throughout the previous decades. Two independent studies, one by Kenneth Greisen [12] and the other by Georgiy Zatsepin and Vadim Kuzmin [13] in 1966 determined that the cause of this cutoff could be due to interactions with

the Cosmic Microwave Background (CMB). Protons above a certain energy threshold interact with photons from the CMB under the following reaction:

$$p + \gamma \rightarrow \Delta^{+} \rightarrow p + \pi^{0} \tag{2.2}$$

$$p + \gamma \rightarrow \Delta^{+} \rightarrow n + \pi^{+} \tag{2.3}$$

each interaction reduces the proton's energy by a fraction of $\Delta E_p / E_p \approx 0.2$ [14] and therefore limits the observed energy from Earth. This was given the name of Greisen-Zatsepin-Kuzmin (GZK) Limit. In order to somewhat accurately determine the GZK cutoff value, one must only calculate the minimum energy required in protons for these reactions to take place. Starting with Eq. 2.2, one needs only to apply conservation of four-momentum (in the center of mass frame) to arrive at the same expression given by Hayakawa and Yamamoto while studying highly energetic γ-rays [15],

$$E_{min} = \frac{m_{\pi^0}\left(m_{\pi^0} + 2M_p\right)}{2\varepsilon(1 + \cos\alpha)} \tag{2.4}$$

where ε is the energy of the photon, m_{π^0} is the mass of the neutral pion, M_p is the mass of the proton and α is the zenith angle of the photon with respect to a head-on collision. For one-dimensional propagation, collision can only occur while head-on ($\alpha = 0$), therefore Eq. 2.4 reduces to:

$$E_{min} = \frac{m_{\pi^0}^2 + 2M_p m_{\pi^0}}{4\varepsilon} \tag{2.5}$$

Similarly, Eq. 2.3 yields a similar result for the minimum energy:

$$E_{min} = \frac{(M_n + m_{\pi^+})^2 - (M_p)^2}{2\varepsilon(1+\cos\alpha)} \tag{2.6}$$

where m_{π^+} is the mass of the positive pion and M_n is the mass of the rest mass of the neutron. All particle masses are known constants, only the photon energy is needed to estimate the GZK threshold. The average energy per photon is given by $k_B T$, and the CMB has an average temperature of 2.725 K [16], so the energy can be taken as

$$\varepsilon = k_B T = 8.617 \times 10^{-5}\,\mathrm{eV\,K^{-1}} \times 2.725\,\mathrm{K} \tag{2.7}$$

$$\varepsilon = 2.348 \times 10^{-10}\,\mathrm{MeV} \tag{2.8}$$

Using this value in Eq. 2.5 yields a minimum energy of 2.888×10^{20} eV for CR protons, similarly, Eq. 2.6 requires a minimum energy of 3.023×10^{20} eV, which is around the same order of magnitude theorized by Greisen, Zatsepin and Kuzmin [12, 13]. The calculations are consistent with observations, as seen in Fig.1, with the cutoff of detected particles at the correct order of magnitude. The precise energy loss over time is discussed in the next section.

2.3 Energy Loss in UHECR propagation

As mentioned in previous Sec. 2.2, one of the main causes of energy loss for UHECR protons are interactions the photon background, mainly with the CMB through Eq. 2.2 and 2.3. However, UHECRs can also interact with other com-

ponents of the electromagnetic spectrum. Following the CMB, CRs usually interact with the Cosmic Infrared Background (CIB or IRB); for energies higher than 10^{20} eV, the contribution is fairly low ($\sim 5\%$), however, for lower energies its contribution is so significant that it lowers the GZK cut-off to $\approx 10^{19}$ eV from the previously calculated 10^{20} eV from Eq. 2.5 and 2.6 [17].

Another common reaction in which protons lose energy in their trajectories is electron pair production through the following process:

$$p + \gamma \rightarrow p + e^{+} + e^{-} \tag{2.9}$$

where the photon γ can come from either the CMB or IRB. In the cases where the remaining protons still posses an energy above the respective reaction threshold, e.g. in Eq 2.2 or Eq 2.9, then the process can repeatedly take place and will continuously drain the proton of energy until it does not have enough to interact with the photon background [18].

The energy loss over time of CR protons interacting with the cosmic photon background is given by

$$-\frac{1}{E}\frac{dE}{dt} = \frac{-ckT}{2\pi^2\Gamma^2(c\hbar)^3}\sum_j \int_{\omega_{0j}}^{\infty} d\omega_r \sigma_j(\omega_r) y_j \omega_r \ln\left(1 - e^{-\omega_r/2\Gamma kT}\right) \tag{2.10}$$

where ω_r is the photon energy in the rest frame of the proton, and y_j is the average fraction of the energy lost by the photon to the proton in the laboratory frame for the j^{th} reaction channel. The sum is carried out over all channels and $d\omega$, σ_j (ω_r) is the total cross section of the j^{th} interaction channel, Γ is the usual Lorentz factor of the proton, and ω_{0j} is the threshold energy for the j^{th}

reaction in the rest frame of the proton [9].

We can solve Eq. 2.10 by making the relevant approximations according to the center of mass energy $s = (\varepsilon + E)^2 = m_p^2 + 2m_p\varepsilon$. For values of $\sqrt{s} < 2\,\text{GeV}$, we can fit the numerical results using the exponential behavior

$$-\frac{1}{E}\frac{dE}{dt} = Ae^{-B/E} \tag{2.11}$$

Evaluating the integral and fitting Eq 2.10 with the corresponding cross section and energy threshold values yields

$$\text{Ei}\,(B/E) = At + \text{Ei}\,(B/E_0) \quad \text{for} \quad 10^{19}\text{eV} \lessapprox E \lessapprox 10^{21}\text{eV} \tag{2.12}$$

where $A = (3.66 \pm 0.08) \times 10^{-8} yr^{-1}$, $B = (2.87 \pm 0.03) \times 10^{20}\text{eV}$ and $\text{Ei}(x)$ is the Exponential Integral [9]. On the other hand, for higher center of mass energies of $\sqrt{s} \gtrapprox 3\,\text{GeV}$, the fractional energy loss is roughly constant

$$-\frac{1}{E}\frac{dE}{dt} = C \tag{2.13}$$

$$E(t) = E_0 e^{-Ct} \quad \text{for} \quad E \gtrapprox 10^{21}\text{eV} \tag{2.14}$$

with $C = (2.42 \pm 0.03) \times 10^{-8} yr^{-1}$. Eq. 2.12 and 2.14 provide a straightforward way to calculate the theoretical energy of a cosmic ray proton given its flight time or mean propagation distance [9, 19]. We can observe the results of the numerical approximation in Fig. 2 with three different initial energies ($10^{20}\,\text{eV}$, $10^{21}\,\text{eV}$, $10^{22}\,\text{eV}$). Note that after a distance of approximately 100 Mpc, or propagation time of 3×10^8 yr, the average observed energy is essentially less

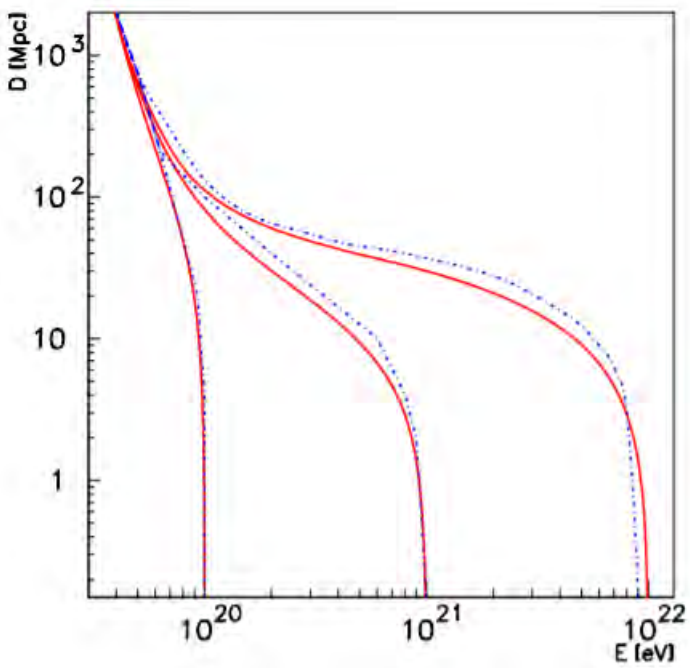

Figure 2: Energy attenuation length of protons in the intergalactic medium. The solid-lines indicate the results from Eq. 2.12 and 2.14 with three different values for initial energy (10^{20} eV, 10^{21} eV, 10^{22} eV), whereas the dashed-lines correspond to the results of a Monte Carlo simulations for the same energies [19].

than 10^{20} eV regardless of the initial value [19], which is consistent with the GZK limit calculations from Sec. 2.2.

The final cause of energy loss in CRs is caused by cosmological effects, primarily by the adiabatic expansion of the universe causing a reduction in the momentum of CRs by a factor of $(1+z)^{-1}$ [20]. The evolution of z is given by

$$\left|\frac{dt}{dz}\right| = \frac{1}{H_0(1+z)\sqrt{\Omega_m(1+z)^3+\Omega_\Lambda}} \tag{2.15}$$

in the standard ΛCDM cosmology, where H_0 is the Hubble parameter at present time ($H_0 \approx 67.3\,\mathrm{km\,s^{-1}\,Mpc^{-1}}$), Ω_m is the density of matter in the universe ($\Omega_m \approx 0.315$), and Ω_Λ is the cosmological constant ($\Omega_\Lambda \approx 0.685$) [21]. In order to calculate these effects, it is necessary to know the propagation distance beforehand. In three-dimensional space this becomes particularly complicated,

as the particle's trajectory is modified by intervening magnetic fields. However, for the one-dimensional propagation studied in this work the initial redshift value is trivial, as it is given by the initial source distance [20].

Chapter 3

Simulations

3.1 CRPropa Simulation Framework

The simulation program for the following work was done with CRPropa, which is a publicly available[1] simulation framework to study the propagation of UHE-CRs (up to iron) on their voyage through an (extra)galactic environment [22]. Simulations are carried out through a collection of modules, which represent the different processes, observers and other aspects of the simulation (source, coordinates, output, etc.). Each module is independent of one another, which allows greater flexibility when defining simulations, as each probability and reaction is calculated independently in each propagation step. Each simulation begins with a single module called `ModuleList`, which acts as a container for all other available modules. Each subsequent module can be added and customized with individual options. As illustrated in Fig. 3, the simulation is carried out performing each individual task separately and sequentially, and only modules that are loaded into the initial `ModuleList` are taken into account for

[1] `https://github.com/CRPropa/CRPropa3`

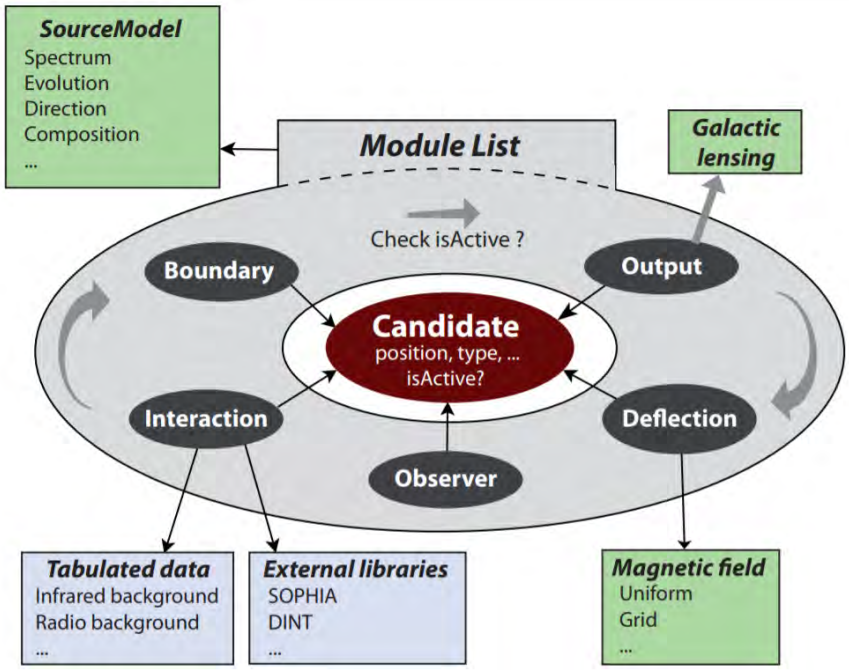

Figure 3: CRPropa 3 modular structure. Each module is independent from the other, and the program checks if each module is active in order to perform additional calculations during each cycle. Some modules can have additional customization options like the ones shown above [20].

the simulation.

For this work, the one-dimensional propagation module `SimplePropagation` was used. To include the processes seen in Chapter 2, one only needs to load the appropriate modules into the simulation. For photopion production, namely Eq. 2.2 and 2.3, only the `PhotoPionProduction` module is needed; similarly, for electron pair production, or Eq. 2.9, the `ElectronPairProduction` module must be used. Both of these modules can be called with the CMB or IRB photon backgrounds to interact with the cosmic rays [22]. The CMB, as previously mentioned, is modelled within CRPropa with a standard blackbody spectrum of temperature $T \approx 2.725\,\mathrm{K}$, whereas the IRB model can be chosen from different available models, by default the Gillmore 2012 infrared model [23] is selected. The cosmological effects from Eq. 2.15 are taken into account by the

`Redshift` module, which obtains the initial redshift value using the source distance as an input. For more complex simulations in three dimensions, CRPropa also includes models of magnetic fields, such as the galactic magnetic field model proposed by Janson and Farrar [24]. Finally, source energy can vary greatly from a specified constant value to a power law distribution with variable maximum and minimum energies, as well as adjustable decay rate; source composition can also be selected, with a random or specified atom composition.

3.2 One-Dimensional Simulations

The initial simulations were done as testing trials for further experiments, so the first objective was to determine the ideal source energy composition. Constant source energy is not representative of real astrophysical sources, so the `SourcePowerLawSpectrum` module was used with a decay rate of E^{-2} to cover different energy ranges. Three simulations were made, the minimum source energy was set to be 1 EeV in all of them, and the maximum energy was varied between 200 EeV, 600 EeV and 1000 EeV. To ensure a large enough sample, one million protons were injected for each of the simulations. For source distance, the `SourceUniform1D` module was used, which spreads out particle emission evenly over the specified distance range, in this case the range was set from 1 Mpc to 1100 Mpc. The results from these runs are shown in Fig. 4.

All three sets of results behave in a similar fashion for lower energy values, and for energies below ≈ 80 EeV they are virtually indistinguishable. The most noticeable feature of the results in Fig. 4 is the sudden disappearance of the

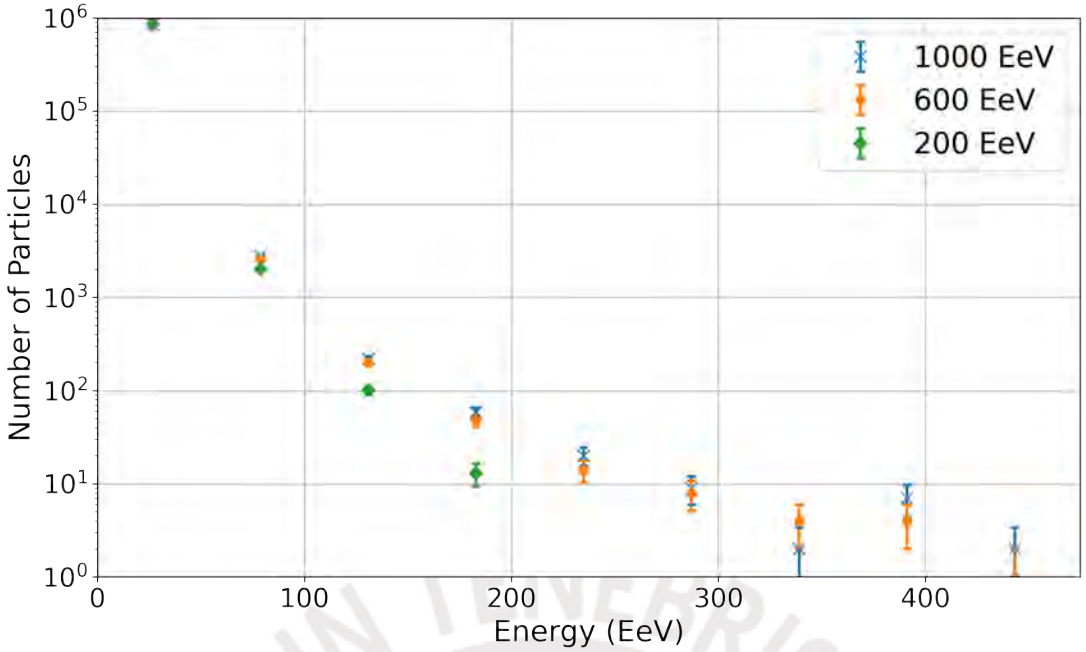

Figure 4: Total detected particles for each simulation. The sets of 600 EeV and 1000 EeV follow a similar pattern, while the 200 EeV set ends at midway.

200 EeV set; this is to be expected, as particles coming from it cannot have an energy above 200 EeV, as it would exceed the allowed maximum. The sets with maximum energies of 600 EeV and 1000 EeV follow the same pattern with little difference between each other, and both show little to no detected particles with energies above 450 Mpc.

The best maximum energy for the simulations cannot be determined through these results alone, further classification of the data is required. With the same particle sets, the GZK limit was evaluated by counting the number of particles arriving with an energy above a certain threshold and registering the distance from where it was emitted. Fig. 5 shows the number of protons above 50 EeV, while Fig. 6 shows the number above 100 EeV. All traces of particles above 50 EeV disappear after approximately 400 Mpc of traveling distance. On the other hand, data with energies above 100 EeV seems to come from much shorter

Table 3.1: Summary of results for the maximum energy trials. Columns 3 and 5 show the number of atoms detected above 50 EeV and 100 EeV, respectively. The relative % column shows the percentage of protons that were detected with respect to the total amount that was emitted above the same energy. The total detected particles are similar for all three trials, while the lowest energy set shows the lowest count for particles above the established energy thresholds.

	Total detected	$E > 50$ EeV	Relative %	$E > 100$ EeV	Relative %
200 EeV	856943	2546	17.0	139	2.8
600 EeV	857129	3357	18.3	325	3.9
1000 EeV	857746	3643	19.2	366	4.1

distances, up until 120 Mpc. This proves to be consistent with Eq. 2.10, that shows that longer flight times on average cause larger energy losses on UHECRs. What is interesting to note, is that for energies above 50 EeV, all three sets follow a very similar downward trend. Once again sets of 600 EeV and 1000 EeV are almost indistinguishable from each other and the set of 200 EeV has lower particle count. However, the difference is not as pronounced as in Fig. 4. The opposite occurs for energies above 100 EeV, where the set of 200 EeV contains approximately half of the particles of the other two sets. This is likely due to the fact that protons coming from this set need to arrive with more than their maximum possible energy (as 200 EeV is the maximum possible) additionally, particles could have been emitted with energies lower than 100 EeV in the first place, as the simulation was not set to a constant energy but rather to a `PowerLaw` distribution. Table 3.1 shows a summary of numbers for each set. All three trials have a similar total number of detections, and a loss of approx 15% of the total emitted particles. The similarities between 600 EeV and 1000 EeV are evident, as both have little difference between the number count, and it comes as no surprise to see the set of 200 EeV with the most difference in the number of highly energetic particles. With all things considered, the ideal

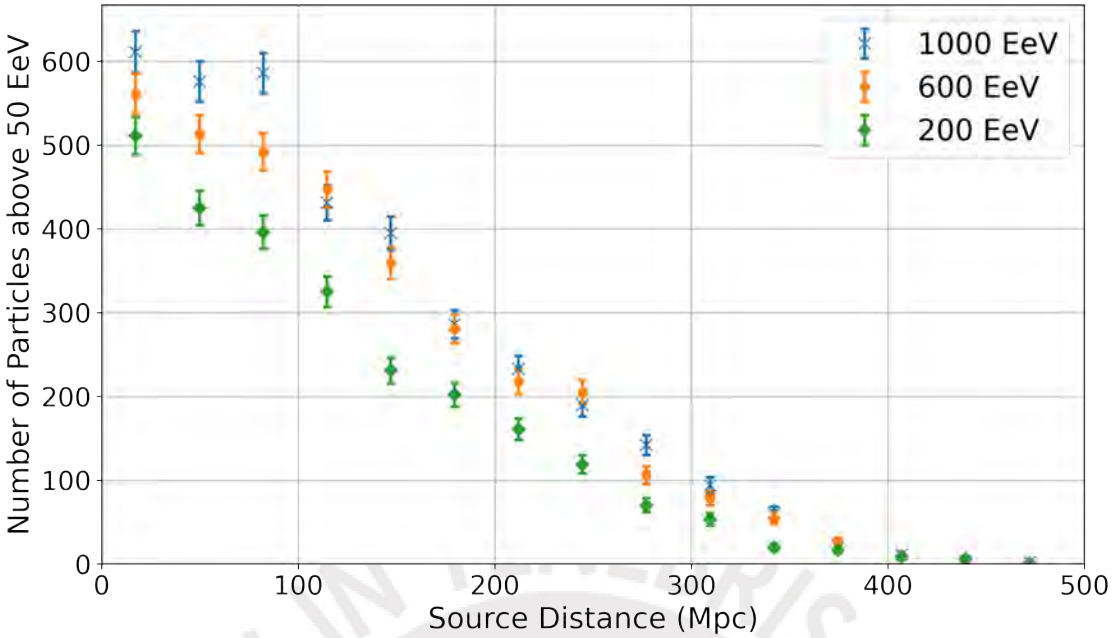

Figure 5: Number of protons detected with energies above 50 EeV or 5×10^{19} eV according to the distance travelled. Lower travelled distances have a higher proton count due to less total interactions with the photon background. For higher distances all three sets appear to slowly converge until they reach zero.

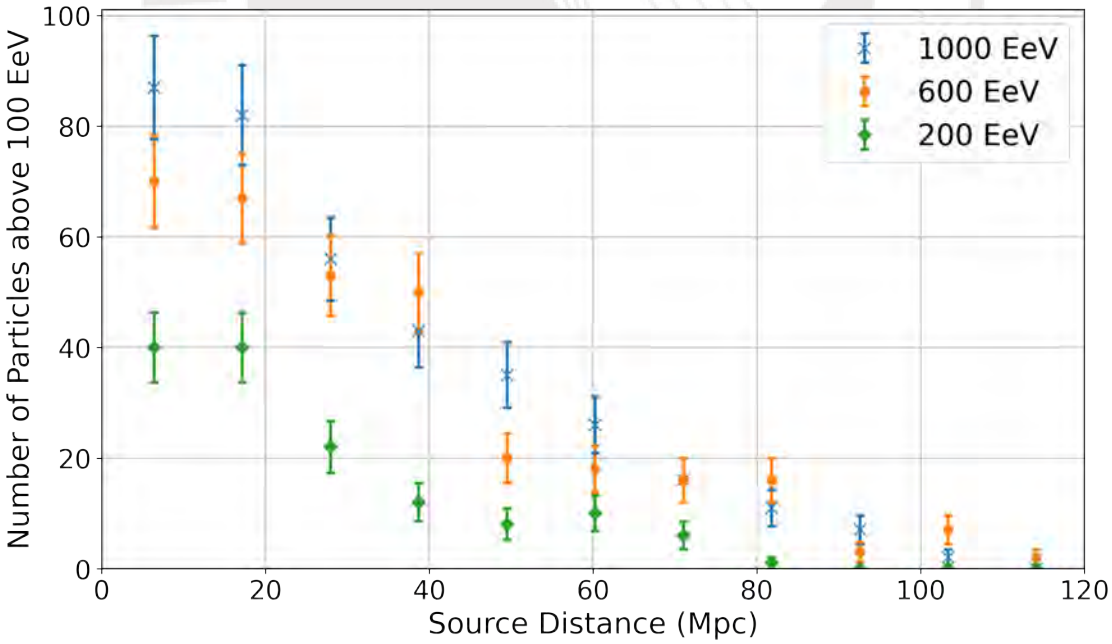

Figure 6: Number of protons detected with energies above 100 EeV or 1×10^{20} eV according to the distance travelled. Overall travel distance is drastically reduced compared to Fig. 5. Only the 600 EeV and 1000 EeV sets are similar; the 200 EeV lacks energy and thus the proton count is almost halved in comparison to the others.

choice for the source maximum energy was chosen to be 600 EeV. The 200 EeV set significantly loses data the further the emission source is, so it will not be taken into account; the 1000 EeV set yields similar results to the 600 EeV, so selecting this set or higher energies would increase simulation workload without any significant increase in returns. From this point onwards all simulations will be done with a maximum possible energy of 600 EeV.

3.3 Energy cutoff for Heavier Nuclei

The second set of simulations was done to observe the effects of the photon background on heavier nuclei, and the simulations were adjusted accordingly. When adding heavier elements into the composition, two new modules must be integrated into the simulations. The first is the `PhotoDisintegration` module, and as the name suggests, it is responsible for the photo-disintegration process. Heavy UHECR nuclei acting with CMB and IRB photons can be stripped of one or more nucleons by

$$(A,Z)+\gamma \rightarrow (A-n,Z-n')+N \tag{3.1}$$

where A is the atomic mass number, Z is the atomic number, n is the number of nucleons lost, and n' is the number of protons lost [25]. N is the new daughter nucleus, which has the same mass number but not necessarily the same atomic number. Since during this process sometimes unstable isotopes are produced, we also need to add the `NuclearDecay` module, which is responsible for making these unstable isotopes disintegrate or split into much smaller components

Table 3.2: Summary of total particles detected by atom type. A total of 10^6 particles was emitted for each set. Heavier elements have lower percentages as photodesintegration splits nucleons apart into smaller atoms.

	Total detected	Relative %
Protons	857468	0.857
Helium	656756	0.657
Nitrogen	589331	0.589
Iron	487115	0.487

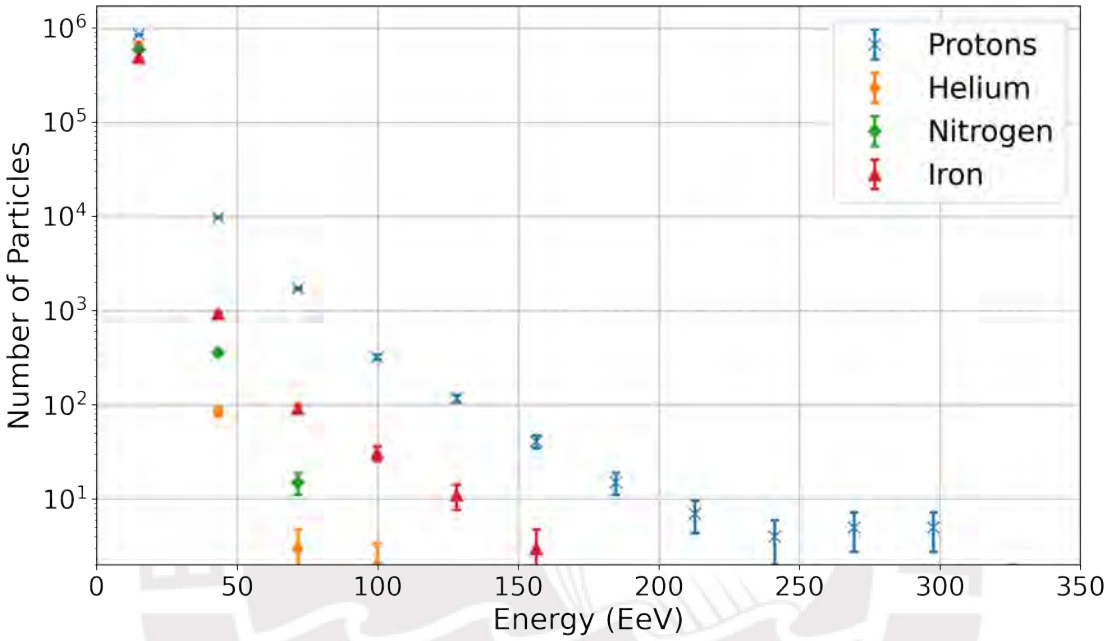

Figure 7: Total number of particles detected per atom type. Protons follow a similar behavior as with Fig. 4. Lighter elements appear to sharply drop, and heavier elements (Iron), become more prominent when observing higher energies.

through the standard α, β and γ decay channels. For simplicity, four sets of monoatomic sources were created: protons, Helium, Nitrogen and Iron were chosen to observe the behavior of different UHECR nuclei propagating through space. In the previous trials, the best maximum possible energy for protons was set to be 600 EeV; for simplicity, the same maximum value will be used for the sets of other atoms, and 10^6 particles will be injected in each set. The results are shown in Fig. 7 and Table 3.2. If we look at Table 3.2, we can easily observe a clear decrease in detection rate as the candidates become heavier. This

occurs because, as elements become heavier, the target size for photon collision becomes larger, increasing the reaction cross section; additionally, the increasing number of nucleons allow for more photo-disintegration channels (that is, more possible combinations on how the nucleus can be split by a single photon) [26]. However, heavy nuclei propagation is not that straightforward. As Fig. 7 shows, even though Iron has the lowest relative detection it still manages to reach the highest available energies (except for protons). This is consistent with previous studies of UHECR flux that show that heavier elements become increasingly prevalent around the ankle [27]; a more precise flux composition will be studied in Chapter 4. In a similar manner to what was done with Fig. 5, the number of particles above 50 EeV was counted, this time separately for each atom. The results of this count is shown in Fig. 8. Out of the four candidates, it is evident that UHECR protons can travel the furthest, and that heavier nuclei have their travel distance drastically reduced. Additionally, one can see further evidence of the increasing presence of Iron for higher energies, as Helium distance is minimal and Nitrogen is barely detected past 20 Mpc. Other studies have reached the same results by examining the photo-disintegration cross section of atoms and the effects of magnetic fields on charged particles, showing that sources for heavier UHECR must be nearer than UHECR protons [28]. Three-dimensional simulations would show further evidence of the reduced travel distance, as it would allow the integration of magnetic fields and particle deflection. An additional test with a threshold above 100 EeV was made, however, counts were too low to provide an accurate graphical representation. The total results of this test are show in Table 3.3, alongside the previous

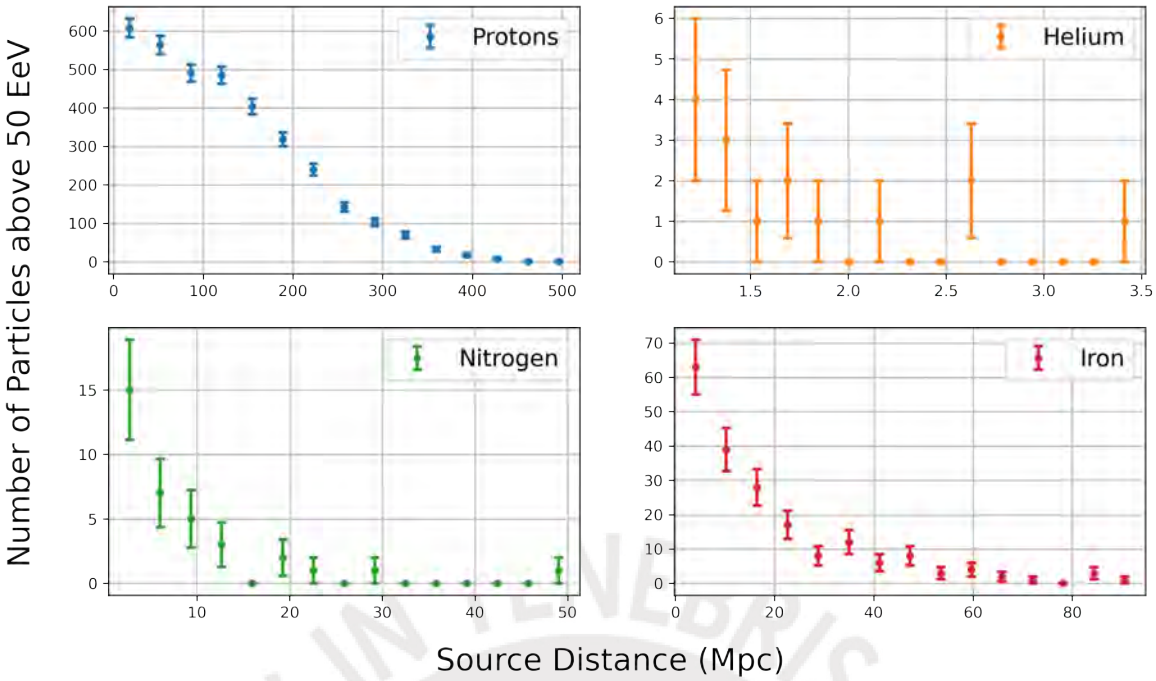

Figure 8: Number of atoms detected with energies above 50 EeV or 5×10^{19} eV according to the distance travelled. Each graph represents a different candidate. Protons presents the largest and smoothest of all the behaviours, similar to Fig. 5, followed by Iron which a considerable decrease in count numbers. Helium has the least number of counts above the threshold, along with incredibly short traveling distances.

total results for comparison.

The results for protons are consistent with what was previously found in Table 3.1. As was previously mentioned, heavy particle count drops considerably, shown with Helium dropping to barely four particles and Nitrogen having no particles above 100 EeV. Iron becomes the only candidate (aside from protons), to present a significant number above the energy threshold, once again showing

Table 3.3: Summary of total count for each atom. Columns 3 and 5 show the number of atoms detected above 50 EeV and 100 EeV, respectively. The relative % column shows the percentage of atoms that were detected with respect to the total amount that was emitted above the same energy.

	Total detected	$E > 50$ EeV	Relative %	$E > 100$ EeV	Relative %
Protons	857468	3488	18.7	327	3.8
Helium	656756	10	1.4×10^{-4}	4	1.2×10^{-4}
Nitrogen	589331	35	1.4×10^{-4}	0	0
Iron	487115	195	5×10^{-4}	26	8.2×10^{-5}

the prevalence of heavier nuclei for higher energies.

Chapter 4

UHECR Composition and Flux

As mentioned in Chapter 1, CR detection is incredibly complex, as the spectrum covers a wide range of energy and the composition is not constant. As useful as all the information extracted in Chapter 3 is for the purpose of this work, it does not provide an accurate reflection of the data obtained by actual measurements (it is unlikely, if not impossible, to find a pure iron source for example). As such, the next benchmark should be to try to replicate the CR spectrum already measured and fitted by other observatories. As an example, we will use the data obtained from The Pierre Auger Collaboration, which can be openly accessed by the public. In their research, they use a combination of both measurements gathered throughout the years and simulation frameworks to model the spectrum and obtain a possible CR composition at different energy intervals. Their measurements required advanced data processing methods; a sequence of four power laws was used to model the raw data, and afterwards simulation runs determined the composition lines which best fitted the data [29, 30], the fit is shown in Fig. 9.

As shown in the figure, some results are significantly different from what was

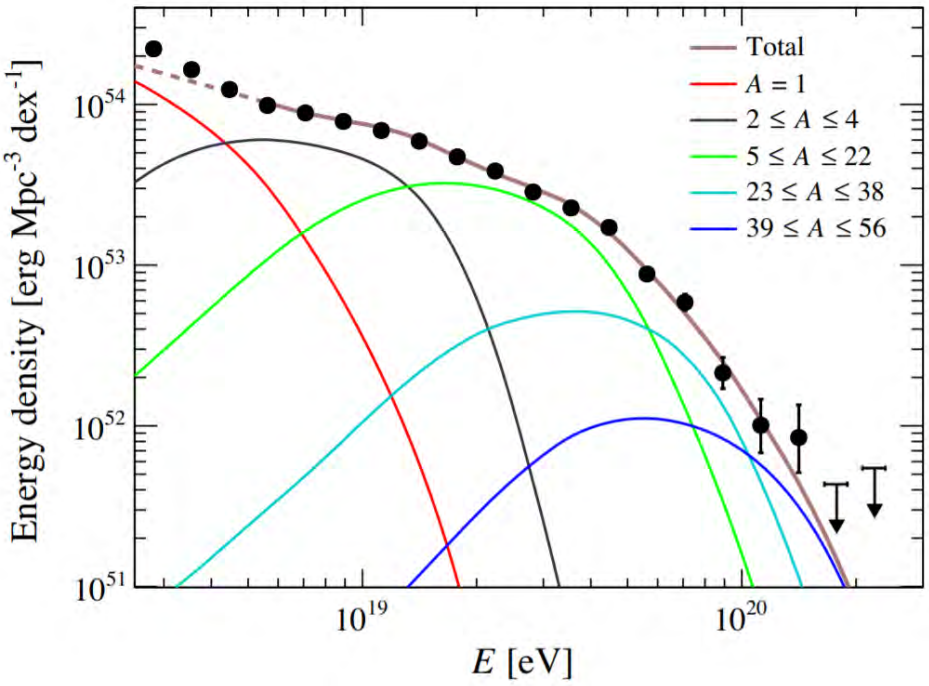

Figure 9: Composition lines created by Pierre-Auger simulations. The black dots represent the raw data measured by the observatory. The colors represent the lines that best fit the data, separated by atomic mass. The dashed curve shows the energy range not included in the fit, as an additional component is required to describe the spectrum [30].

obtained in Chapter 3. Protons for example, reach a maximum energy of $\approx 2 \times 10^{19}$ eV, in contrast to the previous results from Fig. 6 and Fig. 7, which shows protons going to energies above 1×10^{20} eV. Helium has a highly predominant presence below 10^{19} eV and completely disappears by 3×10^{19} eV, whereas in Table 3.3 their numbers are extremely low in comparison, and extend up to 10^{20} eV. Finally, Nitrogen and Iron numbers are much higher in Pierre-Auger's results, which confirms the presence of heavier elements in higher energies.

In order to attempt to recreate a full spectrum like the one in Fig. 9, we need to used a combination of all the previously existing modules, as well as modifying our source to allow multiple nuclei composition; the `SourceMultipleTypes` module allows the addition of multiple nuclei, each with its own relative abun-

dance inside the source. To reach an adequate amount of variety in atomic mass, the composition was divided in five different main atoms. The atoms that were selected were the highest weighted nuclei from each of the five lines in Pierre-Auger's data: Hydrogen ($A = 1$), Helium ($A = 4$), Flourine ($A = 19$), Chlorine ($A = 35$) and Iron ($A = 56$). Two runs with two different sources were made, the first source was built from data extracted from Fig. 9 by using `WebPlotDigitalizer` to pinpoint approximate atom composition values [31], it was composed of 52% protons, 38% Helium, 9.3% Fluorine, 0.5% Chlorine and 0.2% Iron; the second source was made with a more generalized composiiton, taking into account all possible energy ranges [32], and is composed of 89% protons, 10% Helium, and 1% of heavier elements, to keep it consistent with the other source, the percentage of heavier elements was divided into 0.4% Fluorine, 0.3% Chlorine and 0.3% Iron. Results from the Pierre-Auger data are shown in Fig. 10 and results from the generalized spectrum data in Fig. 11. It is important to mention that, while Fig. 9 has units of erg Mpc^{-3} dex^{-1}, both Fig. 10 and Fig. 11 were done with arbitrary units (a.u.) to offer a more generalized result. It is important to note that in both cases (Fig. 10 and 11), protons are extremely predominant despite the composition difference; this is most likely due to the photo-disintegration process discussed in Chapter 3, which knocks off protons off heavier nuclei and creates additional CRs. Heavier elements in both cases seem drop after little over $10^{19}\,\mathrm{eV}$, which is not what data in Fig. 9 shows; this seems to suggest that further analysis of heavier elements is needed to understand this lack of flux for higher energies, most likely a change in the initial energy spectrum is needed, as currently all particles are emitted with the

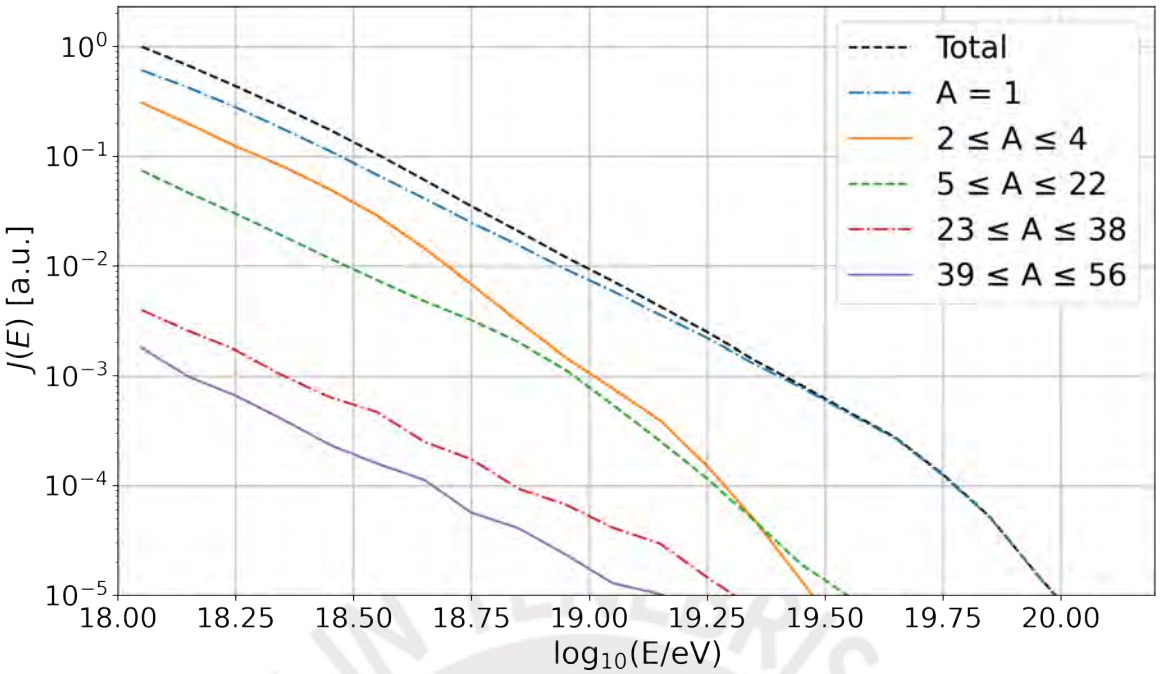

Figure 10: UHECR flux modelled with the composition given by the Pierre-Auger Observatory. Contrary to Fig. 9, heavier element presence drops after 10^{19} eV and lighter elements become dominant.

same power law distribution. Other additional effects, such as the presence of magnetic fields, are not being taken into account as well, as it is not possible to include trajectory deviation in one-dimensional propagation. Both figures seem to suggest that, at least for one-dimensional propagation, source composition is the dominant factor in determining the detected spectrum. Lines in Fig. 10 for example, appear to follow the same pattern as its initial composition, with protons being the highest, followed by Helium, Fluorine, Chlorine and finally Iron. Same applies to Fig. 11, where all three heavier element lines follow a close pattern when given a similar composition percentage, whereas protons and Helium had the highest proportion.

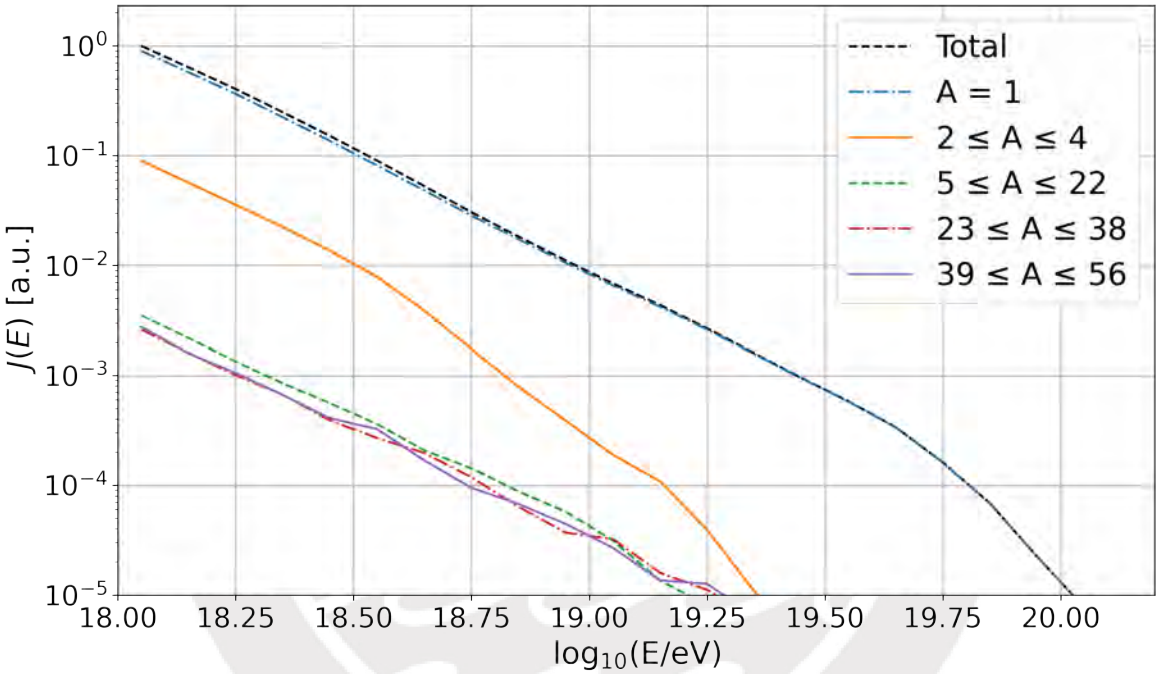

Figure 11: UHECR flux modelled after average CR composition over all energy ranges. Heavier elements follow an almost identical pattern, and protons are shown to compose the majority of the total spectrum.

Chapter 5

Discussion and Conclusions

Throughout the previous chapters, the main interactions and behavior of CRs were studied. The initial runs in Chapter 3 proved useful to visualize and confirm the theory studied previously. The GZK cutoff was verified, along with the effects of different simulation energies in the number of detections. It was found that the simulation with the lowest energy value gives, in return, the lowest particle count. On the other hand, the two simulations with high maximum energy do not seem to give significantly different results from each other, showing that after a certain point increasing maximum energy does not give meaningful results. The effects of the photon background was also observed in heavier nuclei; it can be easily seen how heavy atoms are easily split and disintegrated into smaller particles, explaining why the vast majority of detected CRs are composed of protons.

The most thorough simulation was done in Chapter 4, where a simple model of the UHECR flux was completed. In it, the effects of initial source composition could clearly be observed; the lines of each atomic mass category are heavily influenced by the initial atom composition, and slight changed in it were

reflected in the shape of the spectrum. The ultimate goal of this work was to perform trials and test runs of the CRPropa simulation framework in order to set the basis for future research, and to that extent it was completed successfully. The workings of the framework were learnt in detail and the knowledge is sufficient to start investigating with further and more complex environments.

5.1 Future Work

It is important to remember that all simulations in this work were done with only one-dimensional propagation, and the theoretical background was limited to processes that could only apply in one dimension. When expanding the study to three dimensions for example, one encounters galactic and extragalactic magnetic fields that span the entire propagation medium, introducing CR deflection and further loss of energy. These new and more complex effects could prove crucial in determining a more complete version of the CR spectrum like the results provided by real observatories. Additionally, they allow for the study of different parameters, such as real source locations, or measurement of arrival anisotropy. It must remembered that, when studying real CR propagation, one needs to take into account these and other complex processes and interactions, as such, this work will be the first stepping stone for further investigations on this subject.

Bibliography

[1] D. PACINI, 1912. "La radiazione penetrante alla superficie ed in seno alle acque". *Il Nuovo Cimento 3*(1):93. Translated and commented by Alessandro De Angelis (2017), 1002.1810.

[2] V. F. HESS, 1912. "Measurements of the penetrating radiation during seven balloon flights". *Phys. Z. 13*:1084. Translated and commented by A. De Angelis and C. Arcaro b. Schultz (2018), 1808.02927.

[3] R. MILLIKAN, 1925. "High frequency rays of cosmic origin 1". *Nature 116*:823. URL https://doi.org/10.1038/116823a0.

[4] J. CLAY, 1927. "Penetrating radiation". *Proceedings of the Section of Sciences, Koninklijke Akademie van Wetenschappen Te Amsterdam 30*:1115–1127. URL https://www.dwc.knaw.nl/DL/publications/PU00011919.pdf.

[5] L. ALVAREZ, A. H. COMPTON, 1933. "A positively charged component of cosmic rays". *Phys. Rev. 43*:835. URL https://link.aps.org/doi/10.1103/PhysRev.43.835.

[6] K.-H. KAMPERT, A. A. WATSON, 2012. "Extensive air showers and ultra high-energy cosmic rays: a historical review". *European Physical Journal H 37*(3):359. 1207.4827.

[7] T. ABU-ZAYYAD, ET AL., 2018. "The Knee and the Second Knee of the Cosmic-Ray Energy Spectrum". Submitted to Astroparticle physics, 1803.07052.

[8] P. ZYLA, ET AL. (Particle Data Group), 2020. "Cosmic Rays" *in* "Review of Particle Physics". *PTEP 2020*(8):083C01.

[9] M. T. DOVA, 2013. "Ultra-high energy cosmic rays". En "2013 CERN-Latin-American School of High-Energy Physics, Proceedings", págs. 169–190. URL https://cds.cern.ch/record/2019742/files/169-190\%20Dova.pdf.

[10] J. ABRAHAM, ET AL. (Pierre Auger Collaboration), 2007. "Correlation of the highest energy cosmic rays with nearby extragalactic objects". *Science 318*:938. 0711.2256.

[11] A. AAB, ET AL. (Pierre Auger Collaboration), 2017. "Observation of a Large-scale Anisotropy in the Arrival Directions of Cosmic Rays above 8×10^{18} eV". *Science 357*(6537):1266. 1709.07321.

[12] K. GREISEN, 1966. "End to the cosmic-ray spectrum?" *Phys. Rev. Lett. 16*:748. URL https://link.aps.org/doi/10.1103/PhysRevLett.16.748.

[13] G. T. ZATSEPIN, V. A. KUZ'MIN, 1966. "Upper Limit of the Spectrum of Cosmic Rays". *Soviet Journal of Experimental and Theoretical Physics Letters 4*:78.

[14] A. MÜCKE, ET AL., 1999. "Photohadronic processes in astrophysical environments". *Publications of the Astronomical Society of Australia 16*(2):160.

[15] S. HAYAKAWA, Y. YAMAMOTO, 1963. "Ultra-high energy γ-rays from intergalactic space". *Progress of Theoretical Physics 30*(1):71.

[16] D. J. FIXSEN, 2009. "THE TEMPERATURE OF THE COSMIC MICROWAVE BACKGROUND". *The Astrophysical Journal 707*(2):916. URL `https://doi.org/10.1088/0004-637x/707/2/916`.

[17] E. V. BUGAEV, P. A. KLIMAI, 2007. "Interactions of high energy cosmic rays with extragalactic infrared radiation background". *Phys. Atom. Nucl. 70*:156. `astro-ph/0509395`.

[18] R. ALOISIO, 2017. "Acceleration and propagation of ultra-high energy cosmic rays". *PTEP 2017*(12).

[19] L. A. ANCHORDOQUI, 2019. "Ultra-High-Energy Cosmic Rays". *Phys. Rept. 801*:1. `1807.09645`.

[20] R. A. BATISTA, ET AL., 2016. "Crpropa 3 - a public astrophysical simulation framework for propagating extraterrestrial ultra-high energy particles". *JCAP 2016*(5).

[21] P. ZYLA, ET AL. (Particle Data Group), 2020. "Cosmological Parameters" *in* "Review of Particle Physics". *PTEP 2020*(8):083C01.

[22] R. A. BATISTA, ET AL., 2020. "Crpropa3 documentation". Accessed: January 19, 2021, URL `https://crpropa.github.io/CRPropa3/index.html`.

[23] R. C. GILMORE, ET AL., 2012. "Semi-analytic modelling of the extragalactic background light and consequences for extragalactic gamma-ray spectra". *MNRAS 422*(4):3189.

[24] R. JANSSON, G. R. FARRAR, 2012. "A new model of the galactic magnetic field". *Astrophysical Journal 757*(1).

[25] R. ALOISIO, 2017. "Acceleration and propagation of ultra-high energy cosmic rays". *Progress of Theoretical and Experimental Physics 2017*(12). ISSN 2050-3911. 12A102, `https://academic.oup.com/ptep/article-pdf/2017/12/12A102/22075738/ptx115.pdf`, URL `https://doi.org/10.1093/ptep/ptx115`.

[26] F. STECKER, M. SALAMON, 1999. "Photodisintegration of ultrahigh-energy cosmic rays: A New determination". *Astrophys. J. 512*:521. `astro-ph/9808110`.

[27] M. UNGER, ET AL., 2015. "Origin of the ankle in the ultrahigh energy cosmic ray spectrum, and of the extragalactic protons below it". *Phys. Rev. D. 92*(12).

[28] T. PIRAN, 2010. "A New Limit on the Distances of Nuclei UHECRs Sources" 1005.3311.

[29] A. AAB, ET AL. (Pierre Auger), 2020. "Measurement of the cosmic-ray energy spectrum above 2.5×10^{18} eV using the Pierre Auger Observatory". *Phys. Rev. D 102*(6):062005. 2008.06486.

[30] A. AAB, ET AL. (Pierre Auger), 2020. "Features of the Energy Spectrum of Cosmic Rays above 2.5×10^{18} eV Using the Pierre Auger Observatory". *Phys. Rev. Lett. 125*(12):121106. 2008.06488.

[31] A. ROHATGI. "Webplotdigitalizer version 4.3". https://automeris.io/WebPlotDigitizer. Last Accessed: 12-01-2021.

[32] "Cosmic rays: particles from outer space". https://home.cern/science/physics/cosmic-rays-particles-outer-space. Last Accessed: 11-01-2021.